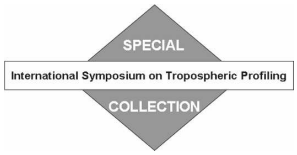

Evaluating the Effects of Height-Variable Reflectivity and Antenna Sidelobes on the Radar Equation

EDWIN F. CAMPOS

Meteorological Research Division, Environment Canada, Toronto, Ontario, Canada

WAYNE HOCKING

Department of Physics, University of Western Ontario, London, Ontario, Canada

FRÉDÉRIC FABRY

Department of Atmospheric and Oceanic Sciences, McGill University, Montreal, Quebec, Canada

(Manuscript received 17 November 2006, in final form 3 August 2007)

ABSTRACT

Using radar observations to quantify precipitation intensity requires the intervention of the radar equation, which converts the precipitation signal into reflectivity units. This equation generally assumes that the reflectivity is uniform within each sampling gate and that the sidelobes of the antenna pattern are negligible. The purpose here is to provide a more realistic approach that eliminates these assumptions when computing profiles of precipitation intensity (by using a height-variable reflectivity and antenna pattern of significant sidelobes to compute profiles of a radar reflectivity factor). To achieve this, simultaneous observations of collocated vertically pointing radars operating in the VHF and X bands were obtained. Raindrop measurements were used to correct for attenuation in the precipitation signal at the X band. Then the precipitation signal in the VHF radar was simulated by combining this X-band signal and the VHF antenna pattern into a general version of the radar equation. The simulated precipitation signal at VHF compares well with actual measurements of the rain signal (range gates centered at 2.5, 3.0, and 3.5 km) by the VHF radar, and this validates the analysis methods. In conclusion, the analysis indicates that VHF reflectivity at gates above the melting layer is artificially enhanced by the precipitation signal collected in the sidelobe direction. Similar enhancement will be expected wherever there is a strong vertical gradient of reflectivity (i.e., on the order of 10 dB km^{-1} or larger).

1. Introduction

Quantitative measurements of meteorological variables by radar imply the use of the radar equation. This is a relationship that links the radar-received power to the scatterers' cross sections. Standard forms for this equation assume, most of the time, an average scatterer cross section per unit volume (or radar reflectivity) that is constant within the sampling volume of a given range gate. Under these conditions and neglecting the effect of the convolution of the transmitted pulse with the reflectivity profile, the radar equation is given by the following expression [for details on its derivation, see Campos et al. (2007); Eq. (18)]:

$$P_r = \frac{P_{\mathrm{Tx}} e_T (D_{\max})^2 \lambda^2 \overline{\eta}}{(4\pi)^3} \left[\frac{L/2}{R^2 - (L/4)^2} \right] \int_{\varphi=0}^{2\pi} \left\{ \int_{\theta=0}^{\pi} [F(\theta, \varphi)]^2 \sin\theta \, d\theta \right\} d\varphi, \quad (1)$$

where P_r is the received power (watts), P_{Tx} is the transmitter power (watts), e_T is the antenna efficiency during pulse transmission, $D_{\max}$ is the maximum directivity of

Corresponding author address: Dr. Edwin Campos, Environment Canada–ARMP/MRD/STB, 4905 Dufferin Street, Toronto, ON M3H 5T4, Canada.
E-mail: edwin.campos@ec.gc.ca

DOI: 10.1175/2007JTECHA941.1

the antenna pattern, λ is the radar transmitted wavelength (meters), $\overline{\eta}$ is the radar reflectivity (m^{-1}) averaged over the sampling volume, F is the one-way normalized polar diagram (or antenna pattern), ϕ is the azimuth angle, θ is the zenith angle, R is the range at the center of a given radar gate (meters), and L is the transmitted pulse length (meters).

Equation (1) is appropriate when dealing with radars that have a narrow transmitted beam and high range resolution. However, this relation may not be valid for radars with an antenna pattern having nonnegligible sidelobes, particularly when the reflectivity field varies strongly in space. The reason is that the radar will receive some of its power from scatterers located at the same distance but at a different angle to the direction of the main beam. [The McGill VHF radar, e.g., has been designed to have the narrowest main beam possible, to facilitate determinations of turbulent energy dissipation rate from spectral widths (i.e., the method described by Hocking 1985, section 7); however, this narrowest main beam results in larger sidelobes.] Therefore, the following radar equation needs to be solved [for details on its derivation, see Campos et al. (2007); Eq. (13)]:

$$P_r = \frac{P_{\mathrm{Tx}} e_T (D_{\max})^2 \lambda^2}{(4\pi)^3} \int_{r=R-L/4}^{R+L/4} \int_{\varphi=0}^{2\pi} \int_{\theta=0}^{\pi} \frac{\eta(r, \theta, \varphi)[F(\theta, \varphi)]^2 \sin\theta}{r^2} \, d\theta \, d\varphi \, dr. \tag{2}$$

The term $r^{-2}\ \eta(r, \theta, \phi)$ inside the previous integral should be, strictly speaking, $[r^{-2}\ \eta(r, \theta, \phi)] \otimes g(r)$, where the symbol $\otimes$ represents a convolution and $g(r)$ describes the transmitted pulse as a function of range r. This analysis, however, will not consider the effects of the pulse shape and will therefore assume a square pulse, such that

$$\frac{\eta(r, \theta, \phi)}{r^2} \otimes g(r) \cong \frac{\eta(r, \theta, \phi)}{r^2}. \tag{3}$$

The effect of the space variability in the reflectivity has been discussed in light of the radar equation (e.g., Hocking and Roettger 1983; Zawadzki 1982; Rogers 1971). However, for tropospheric signals, there are no published analyses of this effect in combination with the sidelobes of an antenna pattern. The objective of this study, then, is to explore the effects of this more realistic approach [i.e., using Eq. (2) in combination with a height-variable reflectivity and with an antenna pattern of nonnegligible sidelobes] when computing profiles of precipitation intensity. The analyses focus on vertical radar observations, particularly from profiling radars such as VHF wind profilers and X-band vertically pointing radars. In this manner, we quantify the power collected by antenna-pattern sidelobes from regions with a strong vertical gradient of reflectivity. The information presented here should be relevant for precipitation applications using radars similar to the McGill VHF profiler.

2. Methods

Recall that the radar reflectivity, for Rayleigh scatterers, can be expressed as [e.g., Rinehart (1997); Eq. (5.13)]

$$\eta = \frac{\pi^5 |K|^2}{\lambda^4} \frac{Z}{10^{18}}, \tag{4}$$

where $|K|^2$ is the dielectric factor and λ is the wavelength of the radar-transmitted pulse (meters). Here, Z is the reflectivity factor ($mm^6\ m^{-3}$), which provides a measure of the precipitation intensity for hydrometeor targets. By convention (e.g., Smith 1984), if $|K|^2$ is taken equal to 0.93 (the value corresponding to liquid water at near 20°C and wavelengths in the S band), then $Z = Z_e$, the equivalent radar reflectivity factor. This convention is adopted because when radar measurements are made, the hydrometeor phase or composition is often not certain (i.e., we are uncertain of the dielectric factor values).

Hence, from an original field of Z_e we can derive a field of η using Eq. (4), and then apply either Eq. (1) or (2) to obtain the radar-received power. Operationally, however, the radar measures received powers, and these have to be converted into equivalent reflectivity factors. This can be done easily from Eq. (1), using $\eta = \overline{\eta}$, but it cannot be done directly if the more realistic Eq. (2) is used (because here η is within the integral).

However, we were able to simulate VHF reflectivity factors through Eq. (2), using as input the precipitation signal at the X band, and validating the simulation with corresponding measurements at the VHF band. Figure 1 summarizes our method. First, a field of Z_e is input into Eq. (4) to obtain η. (We can input here any observed or artificial Z_e field.) At this point, $|K|^2 = 0.93$ is also used. Then, we input this equivalent reflectivity factor into Eq. (2) to obtain a realistic radar-received power (for a given radar range gate). Next, we input the received power from Eq. (2) into Eq. (1) to obtain an

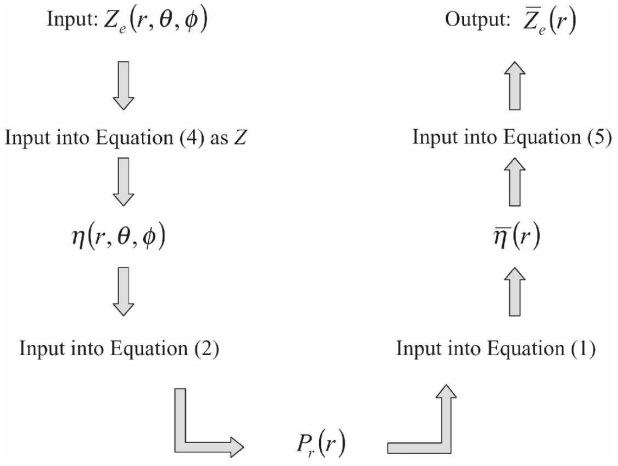

FIG. 1. Flowchart describing the process by which we simulate profiles of an equivalent reflectivity factor at the VHF band. It uses Eq. (2) in combination with a height-variable reflectivity at the X band and with a VHF antenna pattern of nonnegligible sidelobes.

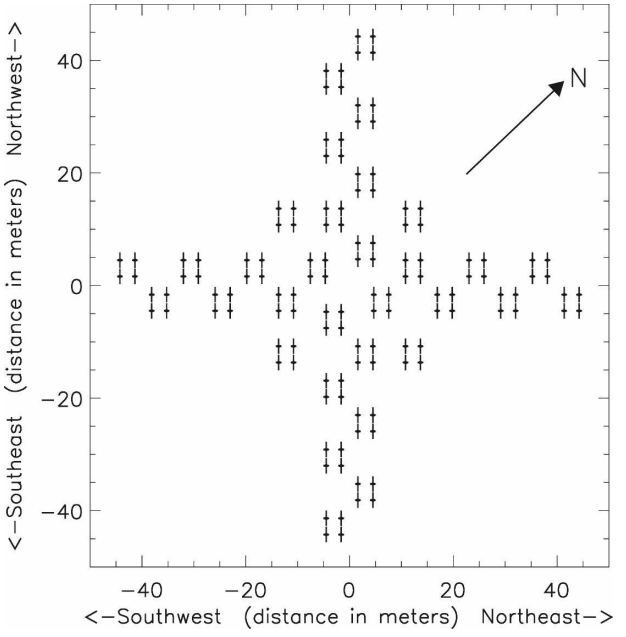

FIG. 2. Plan for the antenna array of the McGill VHF radar. Note that the aerials are aligned at 48.7° from the north.

average (within the radar gate) reflectivity $\overline{\eta}$. An average equivalent reflectivity factor (for the radar gate) is then obtained by rearranging Eq. (4) as

$$\overline{Z}_e = \frac{\lambda^4 10^{18}}{\pi^5 |K|^2}\,\overline{\eta}. \tag{5}$$

The procedure is repeated for all radar range gates. In the end, we are able to compare the output $\overline{Z}_e$ and the original Z_e fields.

For simplicity, we used Z_e fields that were variable only with height z (i.e., one-dimensional fields). This is done for practical reasons because our X-band radar (input dataset) points only vertically. However, it is also a reasonable assumption because the precipitation signals at our radar site (generated mainly by stratiform systems) present a much larger variation in the vertical than in the horizontal. Given this, we would expect that our assumption will be compromised only by particular observations, such as those at the boundaries of convective precipitation. Consequently,

$$\eta = \eta(z) = \eta(r\cos\theta). \tag{6}$$

When applying the method in Fig. 1, we also used the values in Table 1 for the VHF wind profiler. These values correspond to the McGill VHF radar, operating only in a vertical direction. Further description of this radar is given by Campos et al. (2007).

Additionally, we used for $[F(\theta, \phi)]^2$ the values from a numerical simulation of the McGill VHF antenna polar diagram. As input for this simulation, we use the antenna configuration in Fig. 2. The output polar diagram, shown in Fig. 3, was generated using summing of complex (real and imaginary) voltage signals received at each aerial, for an assumed point source at a large distance, well outside the Fresnel region. Source positions were altered from trial to trial until a full coverage of azimuths and zenith angles was achieved. Path differences from the source to each aerial were calculated, and then the appropriate phase delays were calculated and used to determine the received complex voltages. All voltages were then summed. Step sizes for the diagram in Fig. 3 correspond to a 180×180 matrix, but runs with higher resolution were also carried out to examine the detailed structure of the polar diagram close to the main beam. A conducting ground was assumed. Coupling between adjacent aerials is less than -30 dB, thus coupling effects between aerials were not considered. The values in Table 1 were also used.

Notice that the integrals in Eqs. (1) and (2) were computed numerically. Therefore, the accuracy of the programs used for integration required some prior testing (because computations were very sensitive to the antenna pattern resolution). Consequently, we first generated a synthetic Z_e profile that was constant in height (i.e., the vertical dashed line in Fig. 4), put this profile in Eq. (4) to obtain η, input this reflectivity into (2), and solved this equation numerically (i.e., the method in Fig. 1). In principle, the reflectivity factors resulting after numerical integration ($\overline{Z}_e$) have to be the same as the input (Z_e), but this will not be true if the

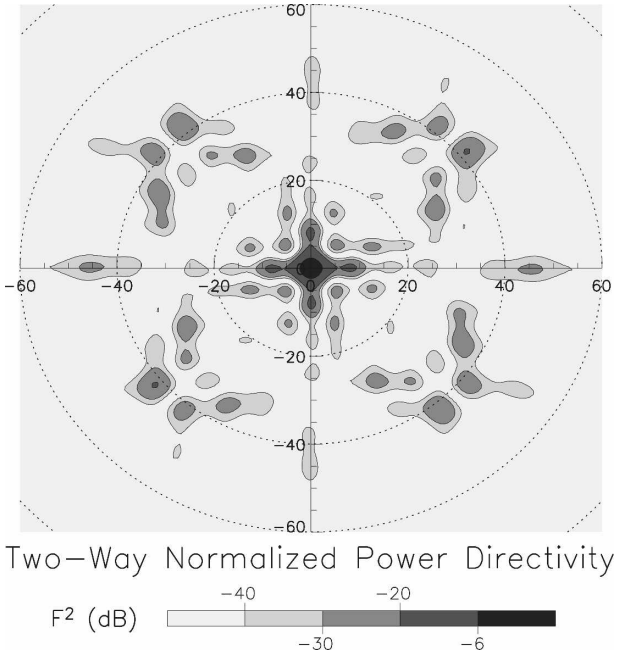

FIG. 3. Two-way antenna pattern (also known as a polar diagram, F^2) for the McGill VHF radar. The concentric circles correspond to the zenith angles in the x and y axes. The azimuth angles start clockwise from the positive y axis. Geographic north is located at 48.7° azimuth.

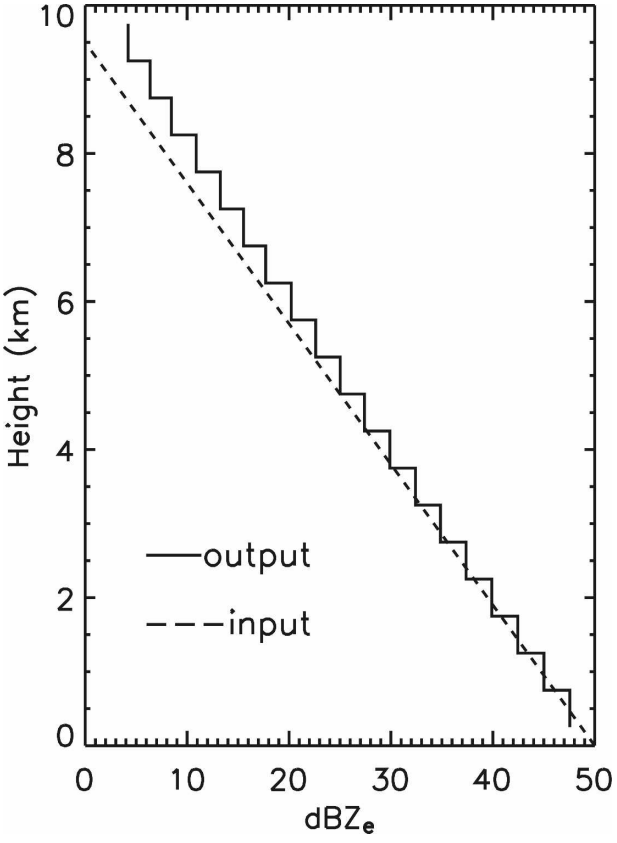

FIG. 4. Simulation of a synthetic Z_e profile. The input profile (dashed line) corresponds to Z_e decreasing with height at 10 dB km^{-1}. The output profile (stepped solid line) corresponds to $\overline{Z}_e$ from the algorithm in Fig. 1.

resolution used is too coarse for an accurate numerical integration. Therefore, we gradually increased the integration resolution until the output $\overline{Z}_e$ equalled the input Z_e.

After validating the integration programs, we generated other different profiles of an equivalent reflectivity factor, and then considered their range variation when computing the $\overline{Z}_e$ values through Eq. (2), which is the method used in Fig. 1. The profiles are made from a 0- to 10-km height, which is the typical range for the troposphere in midlatitudes. The first profile is a synthetic reflectivity factor that decreases exponentially (linearly in decibels) with height. The second profile is an artificial layer of 70 dBZ at a 7-km height, and 0 dBZ everywhere else. The third profile is a synthetic step function, which has a magnitude of 50 dBZ from the ground to a 4-km height, and 0 dBZ aloft.

TABLE 1. Parameters of our collocated, vertically pointing radars.

Value parameter	VHF wind profiler	X-band VPDR
Transmitted wavelength (λ)	5.77 m	3.2 cm
Peak transmitted power (P_{Tx})	40 kW	25 kW
Transmitted pulse length (L)	1 km	150 m
Beamwidth	4.6°	2°
Antenna efficiency (e_T)	63%	Unknown
Maximum directivity (D_{max})	456.9	Unknown

The last profile corresponds to reflectivity factors measured by a high-resolution, vertically pointing X-band radar. This instrument is called the McGill vertically pointing Doppler radar (VPDR; described by Zawadzki et al. 2001). Some relevant parameters of this radar are given in Table 1. To correct for precipitation attenuation at the X band, we collected measurements of raindrop sizes near the ground. For this, we use a Precipitation Occurrence Sensor System (POSS; described by Sheppard 1990), which was collocated with the VPDR and the VHF radars. POSS is a bistatic, X-band (10.5 GHz, 2.85 cm), continuous-wave Doppler radar. This sensor points upward and detects precipitation particles in its sampling volume, which is located only a few centimeters above the instrument (i.e., near ground). (For the various calibration examples comparing raindrop-size measurements and vertically pointing radar observations, the reader is referred to Rogers 1967; Campos and Zawadzki 2000; Gage et al. 2000;

Williams et al. 2005.) The results of our analysis are presented in the next section.

3. Results

The first profile of reflectivity factors, in which a synthetic Z_e decreases with height at 10 dBZ_e km^{-1} (a typical decrease observed in snow over Montreal, QC, Canada), is presented in Fig. 4 as the diagonal dashed line. The corresponding profile of output $\overline{Z}_e$ is also plotted in Fig. 4 as the diagonal stepped line. The results indicate an increase in the $\overline{Z}_e$ slope with height. No significant difference between $\overline{Z}_e$ and Z_e is observed below the 4-km level, but the difference between input and output is greater at higher ranges (reaching about 4 dBZ_e at a 9-km height).

The second profile is plotted as a thick dashed line in Fig. 5. This is a synthetic layer of 70-dBZ magnitude, at a 7-km height, and a 75-m thickness (and 0 dBZ everywhere else). For our numerical simulation, we will assume that this second profile corresponds to a layer present in the whole sampling volume of our VHF radar. The output $\overline{Z}_e$ is plotted as the thick stepped line in Fig. 5, and it shows a broadening on top of the input profile, which extends up to the top of the simulation domain. This result is similar to the ionospheric observations at Adelaide, Australia (35°S, 138°E) by Hocking and Vincent (1982; Fig. 5). In both cases, the spurious signals are due to scatter received through the antenna sidelobes.

The third profile, also plotted in Fig. 5 as a thin dashed line, corresponds to a synthetic step function, which has a magnitude of 50 dBZ from the ground to a 4-km height, and 0 dBZ aloft. This profile is similar to the backscatter signal from a summer rain shower as observed by microwave (centimeter wavelength) radars, where rain rates of similar intensity are present from the base to the top of the cloud. The output $\overline{Z}_e$ is plotted in Fig. 5 as the thin stepped line. The output profile resembles well the input Z_e at heights below 4 km, but the sidelobes receive enough scatter at ranges between 4 and 10 km, such that the output $\overline{Z}_e$ profile is contaminated above 4 km.

We also simulated VHF reflectivity profiles using shorter pulse lengths [i.e., $L < 1$ km in Eqs. (1) and (2)] with the second and third input profiles (dashed lines) in Fig. 5. The results (not shown) are very similar to those with a 1-km pulse length, which indicates that output reflectivities are enhanced at heights above strong vertical gradients of input reflectivity.

A fourth, more realistic profile is presented in Fig. 6, in which the input Z_e is a dashed line and the output $\overline{Z}_e$ is a solid stepped line. For this, we considered height

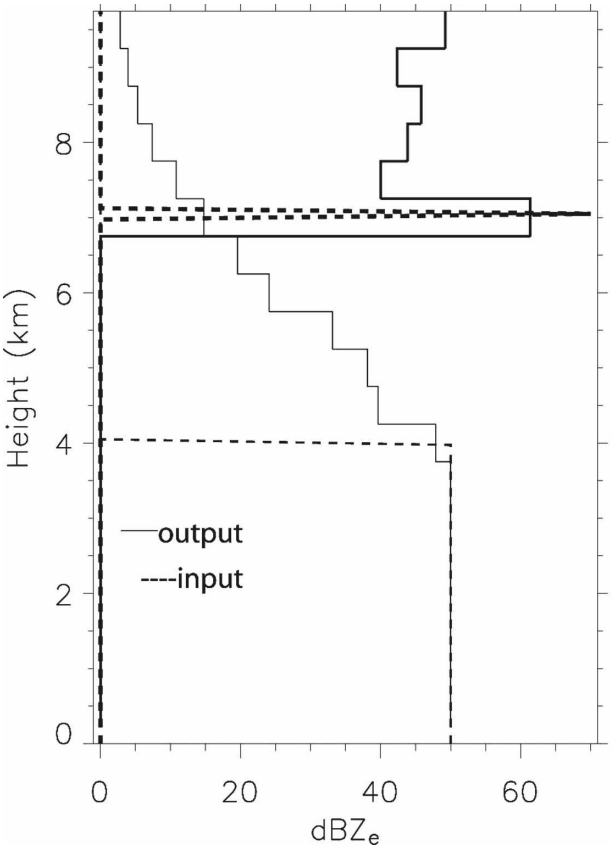

FIG. 5. Additional simulations of synthetic Z_e profiles according to the algorithm in Fig. 1. The first input profile corresponds to a layer of enhanced Z_e at a particular height (thick dashed line; a 70-dBZ layer at a 7-km height). The second input profile corresponds to a region of enhanced, constant Z_e below a particular height (thin dashed line; a 50-dBZ region below the 4-km level). The thick (thin) stepped line is the output $\overline{Z}_e$ profile for the first (second) input profile.

profiles of the equivalent radar reflectivity factor measured by the McGill VPDR radar. The VPDR dataset corresponds to Z_e values at a time resolution of about 30 s and at a range resolution of about 75 m. We smoothed these VPDR measurements by taking, for each particular range gate, the 10-min median value. Notice that $\overline{Z}_e$ is in fact a simulation of the VHF Z_e, which is obtained from the Z_e observations at the X band.

Because the VPDR operates at the X band, precipitation attenuation must be considered. We calibrated the VPDR measurements by comparing the equivalent reflectivity factors measured at the X band and the corresponding values derived from drop size distributions at ground.

To validate our simulation, the rain signal measured by the VHF radar is also plotted as a dotted line in Fig. 6. This rain signal was obtained from the algorithm

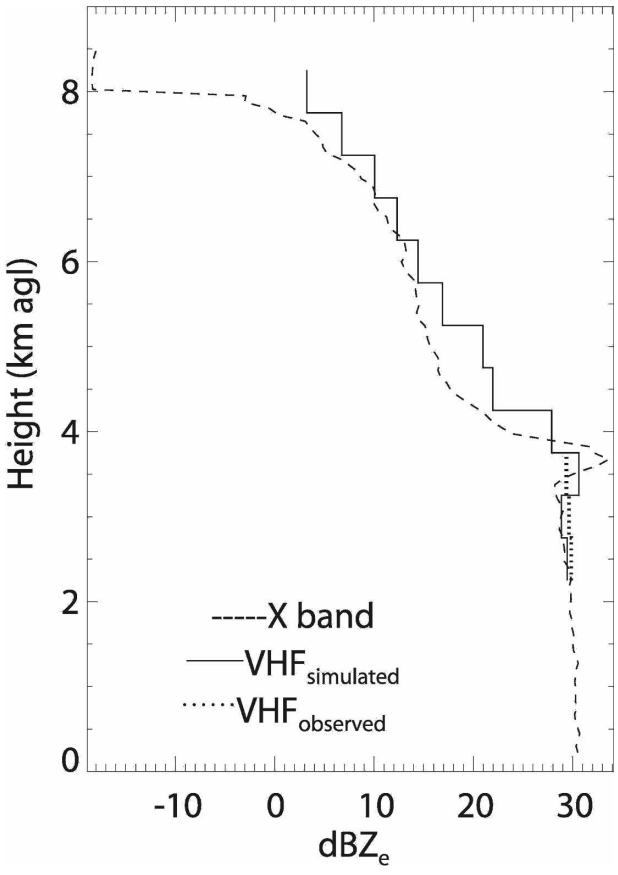

FIG. 6. Simulated VHF $\overline{Z}_e$ profile (solid stepped line) from observed X-band Z_e profile (dashed line, which already includes the attenuation correction). The corresponding VHF observations are plotted as the dotted line: collocated and simultaneous radar observations, at X and VHF bands, were taken at 1300 UTC 9 Sep 2004.

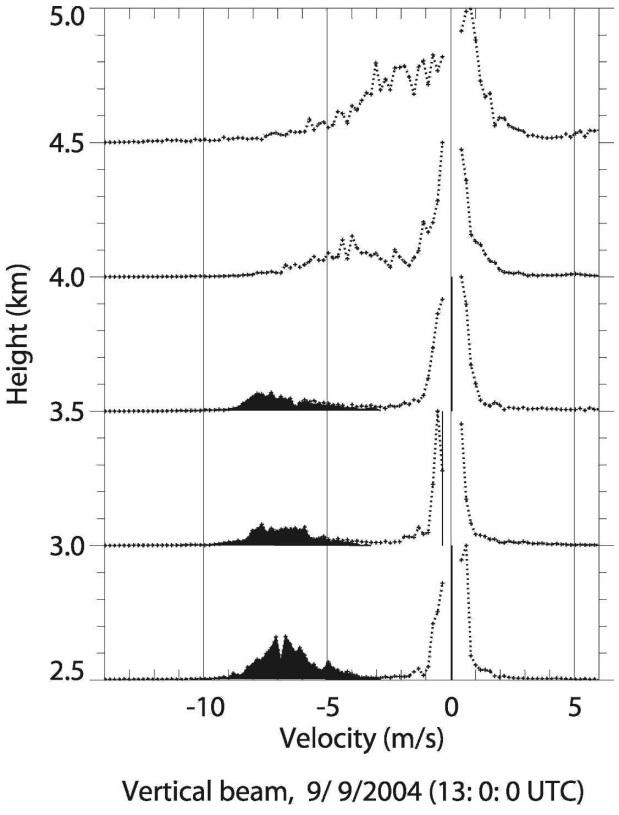

FIG. 7. Vertical profile of reflectivity-factor densities observed by the McGill VHF radar at 1300 UTC 9 Sep 2004. The dotted lines correspond to raw Doppler spectra, and the dark areas below each spectrum correspond to the precipitation signal, according to the algorithm described by Campos et al. (2007). These dark areas relate to the rain Z_e values plotted as dotted lines in Fig. 6. Vertical lines are drawn at the spectral bins corresponding to the clear-air vertical velocities. Above a 3.5-km height, the precipitation is in the solid or melting phase, and the precipitation spectra merge with the clear-air spectra.

described by Campos et al. (2006, section 2.3). The application of this algorithm is presented in Fig. 7 for a profile of Doppler spectra measured by our VHF radar. In these examples, the crosses (linked by dotted curves) correspond to Doppler spectra at different heights, smoothed within a 10-min window. The vertical lines correspond to the air vertical velocities, as the algorithm derives them for each height. The dark areas correspond to the derived precipitation signal. Notice that this algorithm can deal mainly with the precipitation signal coming from ranges up to the bright band, where precipitation spectra are not merged with the clear-air spectra.

4. Discussion

From this analysis, it is found that the height-variable reflectivity has a noticeable effect on the radar equation only above the melting level. Above these heights, the sidelobes of the antenna polar diagram collect enhanced power from scatterers located in the bright band (i.e., ranges in the sidelobe direction corresponding to bright-band height). Similar power enhancement will be expected wherever there is a strong vertical gradient of reflectivity (i.e., on the order of 10 dB km^{-1} or larger; see, e.g., Fig. 4).

For the single profile presented in Fig. 6, the comparison between the simulated and measured VHF rain signals (the dotted and solid lines in Fig. 6, respectively) presents good agreement, which validates our numerical computations. Additionally, these comparisons can be used in a calibration method for VHF stratospheric–tropospheric radars, if the VHF radar observations are expressed in arbitrary units (i.e., the units of the analog-to-digital converter, in the receiver) and if more reflectivity profiles at the X band are analyzed.

From these results, we also expect that rain-only equivalent reflectivity factors will be about the same at X band as at the VHF band (when the X-band measurements are corrected for attenuation). Therefore, it is valid to use Eq. (1) for quantitative measurements of rain by VHF radars. However, the expression (2) must be considered when dealing with snow quantitative measurements at VHF band.

The new approach of using VHF reflectivity to measure rainfall amounts provides several advantages with respect to the more traditional approach of using X-band reflectivity. First, recall that X-band signals often suffer from strong rain attenuation. This is not an issue at the VHF band. Also, calibration of the X-band reflectivity often requires measurements of raindrop sizes, using an additional instrument. VHF-reflectivity calibration, however, does not require any additional instrument if a sky noise method is used (e.g., Campos et al. 2007). In addition, meteorological analyses of precipitation environments can be superior when using VHF radar, instead of using only X-band radar, because vertical air velocities and wind in precipitation-free regions (which are easily obtained using VHF radars) are not possible from X-band observations.

In general, the differences in Z_e from observations at X and VHF bands can be assumed to be due mainly to (i) incorrect radar absolute calibration, (ii) $|K|^2 \neq 0.93$, (iii) effect of the space-variable reflectivity and antenna sidelobes, (iv) inaccurate consideration of the antenna polar diagram F, and (v) nonuniformity of the raindrop field observed by the VHF radar (for implications, see Fabry 1996). In this work, we have already minimized the effects of points (i)–(iv). As a result, no significant differences were found between modeled and observed rain signals.

It falls beyond the objective of this study to correct for the effects of height-variable reflectivity and antenna sidelobes on radar-equation computations. This would imply a specific correction for each particular radar, because the sidelobes in the antenna pattern vary a lot from one radar design to another. We realize, however, that such correction is not needed for most of our VHF rain measurements, because we mostly observe stratiform rain (below the bright band). A correction is also unnecessary for stratiform rain measurements using other systems similar to the McGill VHF radar. A correction can be necessary for cases in which the rain is above a strong vertical gradient of reflectivity (e.g., in upper parts of intense convective storms), but it represents a challenging topic for future consideration.

Various research efforts have attempted to understand the effect of rain on the radio scattering properties of clear air. Some of these studies claim for a reduction of the radio signal in rainy conditions (e.g., McDonald et al. 2004, 2006) while others claim for an enhancement (e.g., Cohn et al. 1995). Unfortunately, those analyses had not considered possible effects from height-variable reflectivity and antenna sidelobes. Consider, for example, shower storms receiving and scattering radiation only from the radar sidelobes (not from the main lobe). This situation can lead to artificial enhancements or reductions in what a signal-processing algorithm identifies as a clear-air signal. Our current study overcomes these inconveniences for rainfall measurements with the McGill VHF radar (and other similar systems). Therefore, we are now able to produce superior analyses about the effect of rain on clear air radio signals (e.g., Campos 2006).

Acknowledgments. The VHF- and X-band radars as well as the POSS distrometer, which we used in this research, are operated and funded by the Marshall Radar Observatory of McGill University.

REFERENCES

Campos, E. F., 2006: Analyses of precipitation signal using VHF vertically pointing radar. Ph.D. dissertation, Dept. of Atmospheric and Oceanic Sciences, McGill University, 188 pp.

——, and I. Zawadzki, 2000: Instrumental uncertainties in *Z–R* relations. *J. Appl. Meteor.,* **39,** 1088–1102.

——, F. Fabry, and W. Hocking, 2007: Precipitation measurements using VHF wind profiler radars: Measuring rainfall and vertical air velocities using only observations with a VHF radar. *Radio Sci.,* **42,** RS3003, doi:10.1029/2006RS003540.

Cohn, S. A., R. R. Rogers, S. Jascourt, W. L. Ecklund, D. A. Carter, and J. S. Wilson, 1995: Interactions between clear-air reflective layers and rain observed with a boundary layer wind profiler. *Radio Sci.,* **30,** 323–341.

Fabry, F., 1996: On the determination of scale ranges for precipitation fields. *J. Geophys. Res.,* **101,** 12 819–12 826.

Gage, K. S., C. R. Williams, P. E. Johnston, W. L. Ecklund, R. Cifelli, A. Tokay, and D. A. Carter, 2000: Doppler radar profilers as calibration tools for scanning radars. *J. Appl. Meteor.,* **39,** 2209–2222.

Hocking, W. K., 1985: Measurement of turbulent energy dissipation rates in the middle atmosphere by radar techniques: A review. *Radio Sci.,* **20,** 1403–1422.

——, and R. A. Vincent, 1982: Comparative observations of D-region HF partial reflections at 2 and 6 MHz. *J. Geophys. Res.,* **87,** 7615–7624.

——, and J. Roettger, 1983: Pulse length dependence of radar signal strengths for Fresnel backscatter. *Radio Sci.,* **18,** 1312–1324.

McDonald, A. J., T. K. Carey-Smith, D. A. Hooper, G. J. Fraser, and B. P. Lublow, 2004: The effect of precipitation on wind-profiler clear air returns. *Ann. Geophys.,* **22,** 3959–3970.

——, K. P. Monahan, D. A. Hooper, and C. Gaffard, 2006: VHF signal power suppression in stratiform and convective precipitation. *Ann. Geophys.,* **24,** 23–35.

Rinehart, R. E., 1997: *Radar for Meteorologist*. 3rd ed. Rinehart Publications, 428 pp.

Rogers, R. R., 1967: Doppler radar investigation of Hawaiian rain. *Tellus,* **19,** 432–455.

——, 1971: The effect of variable target reflectivity on weather radar measurements. *Quart. J. Roy. Meteor. Soc.,* **97,** 154–167.

Sheppard, B. E., 1990: Measurement of raindrop size distributions using a small Doppler radar. *J. Atmos. Oceanic Technol.,* **7,** 255–268.

Smith, P. L., 1984: Equivalent radar reflectivity factors for snow and ice particles. *J. Climate Appl. Meteor.,* **23,** 1258–1260.

Williams, C. R., K. S. Gage, W. Clark, and P. Kucera, 2005: Monitoring the reflectivity calibration of a scanning radar using a profiling radar and a disdrometer. *J. Atmos. Oceanic Technol.,* **22,** 1004–1018.

Zawadzki, I., 1982: The quantitative interpretation of weather radar measurements. *Atmos.–Ocean,* **20,** 158–180.

——, F. Fabry, and W. Szyrmer, 2001: Observations of supercooled water and secondary ice generation by a vertically pointing X-band Doppler radar. *Atmos. Res.,* **59–60,** 343–359.